Highly efficient electrocatalyst of single metal atom doped 2D WS2 for ORR and OER

Linhao Ma
Beijing University of Technology
Ming Zhang (mzhang@bjut.edu.cn)
Beijing University of Technology
Kai Peng
Beijing University of Technology
YuQing Liu
Beijing University of Technology
Junjie Zhao
Beijing University of Technology
Ruzhi Wang
Beijing University of Technology

Research Article

Keywords: electrocatalyst, ORR, OER, Tungsten disulfide, DFT

Posted Date: October 20th, 2023

DOI: https://doi.org/10.21203/rs.3.rs-3455092/v1

Additional Declarations: No competing interests reported.

Highly efficient electrocatalyst of single metal atom doped 2D WS_2 for ORR and OER

Linhao Ma[†‡], Ming Zhang[*†‡], Kai Peng[†‡], Yuqing Liu[†‡], Junjie Zhao[†‡], Ruzhi Wang[†‡]

[†]The Key Laboratory of Advanced Functional Materials, Ministry of Education of China, Beijing University of Technology, Beijing 100124, People's Republic of China

[‡]Faculty of Materials and Manufacturing, Beijing University of Technology, Beijing 100124, People's Republic of China

Abstract

To search for efficient electrocatalyst towards ORR and OER for sustainable energy conversion, storage, and utilization, a family of single transition-metal atom (Mn, Fe, Co, Ni, Cu and Zn) doped two-dimensional tungsten disulfide monolayers have been systematically investigated by using first-principle computations to uncover the impact of transition-metal dopants on ORR and OER electrocatalytic activities. It is demonstrated that single-metal-atom sites can bind to the surface of 2D WS_2, enhancing the adsorption of intermediates involved in the OER/ORR and decreasing overpotentials effectively. Compared to the pristine 2D WS_2, most of transition-metal doped catalysts can decrease overpotentials and promote OER and ORR activities

[*] Correspondence: mzhang@bjut.edu.cn

effectively. Particularly, Ni@WS_2 and Zn@WS_2 are screened out to exhibit the best electrocatalytic activity among all systems with an overpotential of 0.33 and 0.47 V for OER process, respectively, showing that Ni@WS_2 and Zn@WS_2 are potential candidates for OER electrocatalysts. Furthermore, their electrocatalytic performance are explained in terms of volcano plot, scaling diagram, *d*-band center model, and charge analysis.

Keywords: electrocatalyst; ORR; OER; Tungsten disulfide; DFT

Contact address: The Faculty of Materials and Manufacturing，

Beijing University of Technology,

100124, Beijing, P. R. China

E-mail: mzhang@bjut.edu.cn

1. Introduction

Due to the fact that the large-scale exploitation of conventional fossil energy (*i.e.*, coal and petroleum) is extremely harmful to the environment by pollution. Nowadays, searching for effective, renewable and clean energies has attracted extensive attention and interest [1-6]. The proton exchange membrane fuel cells (PEMFCs) and rechargeable metal-air batteries, which performances strongly depend on the oxygen evolution (OER) and/or oxygen reduction reactions (ORR) [7-9], are some of the most promising solutions for meeting future energy demands of electric vehicles, solar cells, *etc*. Nowadays, the exploration of an excellent catalyst for PEMFCs is in full swing. Unfortunately, high cost is still the biggest challenge in marketing PEMFCs for some precious Pt-based electrocatalysts [10-13]. Therefore, the design and development of cost-effective, sustainable, and efficient catalysts is greatly important and urgently desired.

Recently, single-atom electrocatalysts have drawn much attention since the corresponding concept was first proposed by Zhang *et al* in 2011 [14], various single-atom electrocatalysts, such as Mn-N_4, graphene-embedded Fe-N_4, Ni-N_4, Co-N/C, Cu-N/C, Zn-N/C [15-19], have been extensively explored for the OER/ORR due to their high catalytic performance, the maximum atom utilization efficiency and the dramatical reduction in the use of precious metal. However, the tendency of aggregation is an important issue affecting their

performance. The stability of single-atom electrocatalysts has become an ongoing debate and is a large obstacle for their practical applications. Fortunately, it was reported that the isolated metal atoms can be fixed through covalent and electronic interactions with the supports [20], and the catalytic activity can be boosted through the modulation of the morphology and electronic structure of isolated metal atoms by supports as well [21]. Recently, earth abundant two-dimensional transition-metal-dichalcogenides (2D TMDs), such as MoS_2, have attracted great attention for their attractive electronic and electrocatalytic properties [22-24]. Among them, the tungsten disulfide (WS_2) has gained more and more attention and revealed the excellent performance in hydrogen evolution reactions (HER) and OER due to its excellent methanol tolerance and strong stability [25-26]. Additionally, WS_2 is prone to chemical exfoliation and likely to be more suitable for large-scale catalyst applications. However, pristine 2D TMDs generally exhibit low catalytic activity due to their catalytically inert basal surface, poor electric conductivity, and limited active sites. Several techniques, such as nanostructure, defect, interface, and strain engineering, have been developed to generate high catalytic performance for TMD-based materials [27-29]. One of the promising ways is to dope single metal atom, acting as an active site to boost catalytic activity. To our knowledge, enhancing the ORR or OER catalytic activities of 2D WS_2 by the decoration of single transition metal atom

have not been reported yet.

This encourages us to evaluate single transition-metal adatom (STMA) (*M* = Mn, Fe, Co, Ni, Cu, and Zn) doped 2D WS_2 materials (denoted as *M*@WS_2) as ORR and/or OER electrocatalysts by density functional theory (DFT) calculations in this work. Firstly, we found that limited active sites and poor conductivity attributed to its semiconductor nature with a band gap of about 1.62 eV, hindering its catalytic performance for the pristine 2D WS_2 monolayer. By analyzing the adsorption configuration and the adsorption energy of possible oxygenated intermediates including *OOH, *O, and *OH, the scaling linear relationship is evidently approved and a volcano curve correlated between electrocatalytic activity and ΔG_{*OH} is derived, which can be used to quickly screen out STMA doped 2D monolayer WS_2 catalysts with pronounced ORR/OER activities. It is demonstrated that the overpotentials of *M*@WS_2 can be greatly reduced compared with that of the pristine 2D WS_2. Especially, Ni@WS_2 and Zn@WS_2 are screened out to exhibit low overpotentials of around 0.33 and 0.47 V for the OER process, which is slightly better than (or at least compatible to) that of the IrO_2 catalyst (~ 0.40 V). Our findings in this study are expected to stimulate the design of novel and highly efficient non-precious ORR/OER catalysts.

2. Methodology and computational details

The ORR in the acidic medium can be described as

$$O_2 + 4H^+ + 4e^- \rightarrow 2H_2O \quad (1)$$

The elementary steps are as follows according to $4e^-$ pathway

$$*O_2 + H^+ + e^- \leftrightarrow *OOH \quad (2)$$

$$*OOH + H^+ + e^- \leftrightarrow *O + H_2O \quad (3)$$

$$*O + H^+ + e^- \leftrightarrow *OH \quad (4)$$

$$*OH + H^+ + e^- \leftrightarrow * + H_2O \quad (5)$$

where the * denotes the adsorption site.

According to the previous literature, the steady-state adsorption of molecular O_2 on the surface of catalyst does not contribute to the potential dependence of the faradic current when this process is viewed as a chemical step, and the molecular levels of adsorbed O_2 couple to the metal electrons so strongly that electron transfer is unlikely to be rate limiting for the O_2 adsorption. Moreover, because the free energy of O_2 molecule is poorly described by DFT calculations due to its high spin ground state nature, the reaction free energies can be calculated by Eqn. (6)-(8) in order not to calculate the free energy of O_2 directly.

$$* + 2H_2O \leftrightarrow *OOH + 3/2H_2 \quad (6)$$

$$* + H_2O \leftrightarrow *O + H_2 \quad (7)$$

$$* + H_2O \leftrightarrow *OH + 1/2H_2 \quad (8)$$

Then, the adsorption free energy of *O, *OH, and *OOH can be defined as

$$\Delta G_{*O} = G_{H_2} + G_{*O} - G_{H_2O} - G_{*} \quad (9)$$

$$\Delta G_{*OOH} = 1.5G_{H_2} + G_{*OOH} - 2G_{H_2O} - G_{*} \quad (10)$$

$$\Delta G_{*OH} = 0.5G_{H_2} + G_{*OH} - G_{H_2O} - G_{*} \quad (11)$$

At the equilibrium potential of 1.23 V, the reaction free energy of Eqn. (1) is 4.92 eV. Thus, according to Eqn. (9) - (11), the reaction free energy (ΔG_i, i=1, 2, 3, 4) can be defined by the adsorption free energies of ΔG_{*OOH}, ΔG_{*O}, and ΔG_{*OH} as

$$\Delta G_1 = \Delta G_{*OOH} - 4.92 + eU \quad (12)$$

$$\Delta G_2 = \Delta G_{*O} - \Delta G_{*OOH} + eU \quad (13)$$

$$\Delta G_3 = \Delta G_{*OH} - \Delta G_{*O} + eU \quad (14)$$

$$\Delta G_4 = - \Delta G_{*OH} + eU \quad (15)$$

Thus, the thermodynamic limiting potential (U_L) can be calculated by $U_L = -$ max (ΔG_1, ΔG_2, ΔG_3, ΔG_4)/e [30]. Therefore, the theoretical overpotential (η_{ORR}) is defined by [η_{ORR} = max (ΔG_1, ΔG_2, ΔG_3, ΔG_4)/e + 1.23].

The $4e^-$ OER process takes the reverse reaction steps of the ORR. Similarly, (ΔG_i' i = 1, 2, 3, and 4), the change for these OER elementary reaction steps, can be defined as

$$\Delta G_1' = \Delta G_{*OH} - eU \quad (16)$$

$$\Delta G_2' = \Delta G_{*O} - \Delta G_{*OH} - eU \quad (17)$$

$$\Delta G_3' = \Delta G_{*OOH} - \Delta G_{*O} - eU \quad (18)$$

$$\Delta G_4' = 4.92 - \Delta G_{*OOH} - eU \quad (19)$$

The overpotential (η_{OER}) can be calculated by [η_{OER} = max(ΔG_1', ΔG_2', ΔG_3', ΔG_4')/e - 1.23].

In this work, the Gibbs free energy change (ΔG) of each reaction step can be calculated by using the computational hydrogen electrode (CHE) model proposed by Nørskov *et al*. via Eqn. (20) [31],

$$\mathrm{G} = \Delta\mathrm{E} + \Delta\mathrm{ZEP} - \mathrm{T}\Delta\mathrm{S} + \Delta\mathrm{G_p H} + \Delta\mathrm{G_U} \quad (20)$$

where ΔE represents the change of reaction energy that can be directly obtained by DFT calculations. ΔZPE, ΔS, and T are the difference in zero-point energy, that of entropy, and the temperature (298.15 K in this work), respectively. ΔG_U = -eU, which is the change in free energy caused by variations of the electrode potential where U is the bias voltage applied on the electrode. ΔG_{pH} = -$k_B T$ln[H^+], representing Gibbs free energy correction by the H^+ concentration. Herein, pH was set to be zero for acidic medium.

In this work, all calculations are performed based on the first-principles density functional theory (DFT) formalism utilizing the Vienna *ab initio* simulation package (VASP) with the projector augmented wave (PAW) method [32]. The generalized gradient approximation (GGA) is employed to describe the exchange correlation functional using the Perdew-Burke-Ernzerhof (PBE) functional [33]. The cutoff energy is fixed at 450 eV for all calculations to ensure convergence and calculation accuracy. The Brillouin zone is sampled by 3×3×1 k-points. The energy and force values (below 10^{-5}

eV and 0.01 eVÅ^{-1}) were applied on each ion as the criteria for geometry optimizations. The 2D WS_2 catalyst was modelled by 4×4 supercell including 48 atoms. A vacuum space of 20 Å was set in the *z*-direction, which is large enough to avoid interactions between neighboring WS_2 layers. The lattice parameters of the relaxed 2D WS_2 are shown in Table 1.

Table 1 The lattice parameters of the relaxed 2D WS_2 and *M*@WS_2

Catalysts	α (°)	β (°)	γ (°)	*a* (Å)	*b* (Å)	*c* (Å)
WS_2	90.00	90.00	120.00	12.74	12.74	3.14
Mn-WS_2	90.20	89.94	120.01	12.74	12.73	4.68
Fe-WS_2	90.01	89.86	120.00	12.74	12.75	4.16
Co-WS_2	89.95	90.02	120.05	12.75	12.73	4.13
Ni-WS_2	90.08	90.01	120.00	12.74	12.74	4.12
Cu-WS_2	90.38	89.41	120.00	12.68	12.68	4.48
Zn-WS_2	89.67	90.01	120.01	12.73	12.73	5.09

3. Results and discussions

3.1. Stabilities of the STMA doped 2D WS_2

All possible surface adsorption sites of the transition metal atom on 2D WS_2 surface, including the top of W and S atoms, and the center of the membered ring named as W-top, S-top and Cav, are taken into consideration, respectively. All *M*@WS_2 structures are fully relaxed and the relaxed lattice parameters are tabulated in Table 1. Based on the calculated total energies depicted in Figure 1, one can see that all investigated metals prefer to be

adsorbed on the W-top site. In this regard, only W-top configuration is considered for all M@WS_2 systems in the subsequent work.

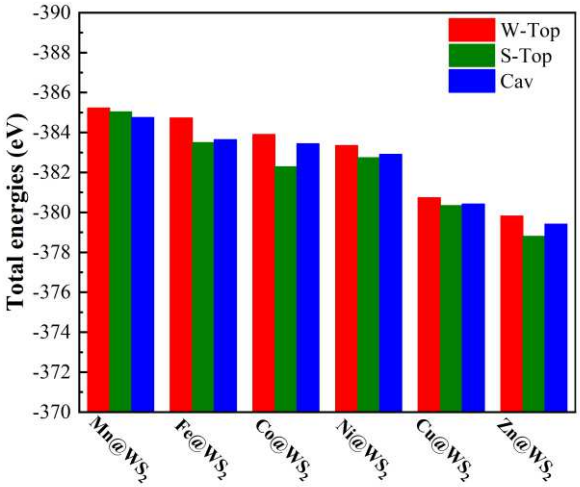

Figure. 1 The total energies of W-top, S-top, and Cav configurations with the transition metal atom at different adsorption sites for the M@WS_2 (M = Mn, Fe, Co, Ni, Cu, and Zn).

Nest, the binding energies (E_b) between STMA and the WS_2 are calculated according to Eqn. (21) [34],

$$E_b = E_{Tot}(M@WS_2) - E_{Tot}(M) - E_{Tot}(WS_2) \qquad (21)$$

where $E_{Tot}(M@WS_2)$, $E_{Tot}(M)$, and $E_{Tot}(WS_2)$ represent the total energies of M@WS_2, the single M atom, and the WS_2, respectively. It is known that the more negative the binding energy, the more stable the adsorption of the metal atom on the support. As shown in Table 2, the binding energies of the transition metal-doped WS_2 monolayer are in the range of -0.16 to -3.17 eV, indicating that all transition atoms such as Mn, Fe, Co, Ni,

Cu, and Zn can thermodynamically bind to the surface of 2D monolayer WS_2.

Table 2 The binding energies (E_b), the adsorption free energy changes (ΔG_{*OOH}, ΔG_{*O}, and ΔG_{*OH}) of different reaction intermediates, the reaction free energy (ΔG_i, i =1, 2, 3, and 4, calculated by Eqn. (12) – (15) at U = 0 V) of the ORR, and calculated overpotential (η) for M@WS_2 (M = Mn, Fe, Co, Ni, Cu, and Zn)

Catalyst	E_b/eV	Gibb's free energies (eV)			ΔG_1	ΔG_2	ΔG_3	ΔG_4	η_{ORR}	η_{OER}
		ΔG_{*OOH}	ΔG_{*O}	ΔG_{*OH}	(eV)	(eV)	(eV)	(eV)	(V)	(V)
WS_2	-	5.08	2.07	2.76	0.16	-3.01	0.69	-2.76	1.91	1.78
Mn-WS_2	-0.63	2.37	-0.09	-1.08	-2.55	-2.46	-0.99	1.08	2.31	1.32
Fe-WS_2	-2.11	2.87	0.57	-0.62	-2.05	-2.30	-1.19	0.62	1.85	1.07
Co-WS_2	-2.52	2.93	0.84	-0.30	-1.99	-2.09	-1.14	0.30	1.53	0.86
Ni-WS_2	-3.17	3.57	2.02	0.59	-1.35	-1.56	-1.43	-0.59	0.64	0.33
Cu-WS_2	-1.05	3.08	1.99	-0.28	-1.84	-1.09	-2.28	0.28	1.51	1.05
Zn-WS_2	-0.16	4.30	2.74	1.04	-0.62	-1.55	-1.70	-1.04	0.61	0.47

3.2. Adsorption of intermediates

The adsorption of the intermediates, such as OH, OOH, O, O_2, HOOH, and H_2O, on the catalyst surface plays an important role in the ORR and OER. In this work, it is demonstrated by the absorption energy calculations (not shown here) that all intermediates such as OH, OOH, O, O_2, and H_2O prefer to adsorb on the top of single transition-metal atom (STMA) rather than the W or S site of WS_2, and the relaxed structures with intermediates adsorbed on M@WS_2 catalysts are shown in Figure 2. Especially, O_2 molecule is usually adsorbed on catalyst surface with two different adsorption configurations

such as side-on and end-on configurations [35]. In this work, O_2 molecule prefers to be adsorbed on STMA site with side-on configuration for all *M*@WS_2 catalysts. Two non-equivalent bonds are formed while O_2 is adsorbed on Co@WS_2, Cu@WS_2 and Zn@WS_2. Thus, two unequal bond lengths are around 0.190 and 0.179 nm for Co@WS_2, 0.195 and 0.190 nm for Cu@WS_2, and 0.174 and 0.191 nm for Zn@WS_2, respectively. For other cases, the formed two bonds are almost equivalent with nearly equal bond lengths, which is about 0.183 nm for Mn@WS_2 and Fe@WS_2, and 0.190 nm for Ni@WS_2, respectively. The bond length between two O atoms of O_2 is elongated from 0.123 to 0.142, 0.138, 0.136, 0.135, 0.133, and 0.132 nm for Mn@WS_2, Fe@WS_2, Co@WS_2, Ni@WS_2, Cu@WS_2, and Zn@WS_2, respectively, indicating that the O2 molecule is activated since the side-on adsorption of O2 on M@WS2 surfaces weakens O-O bonding. Additionally, the O-O bond length decreases with gradually increasing the number of the *d* electron and following the trend of Mn, Fe, Co, Ni, Cu, and Zn, which agrees with the theory proposed by Bockris *et al* [36]. Similarly, the doped Mn, Fe, Co, Ni, Cu, and Zn sites act as the active center for all *OOH, *O, and *OH adsorptions. It is noteworthy that OOH prefers to be adsorbed at the doped STMA site with side-on configuration for Mn@WS_2 and Fe@WS_2, and with end-on configuration for other cases.

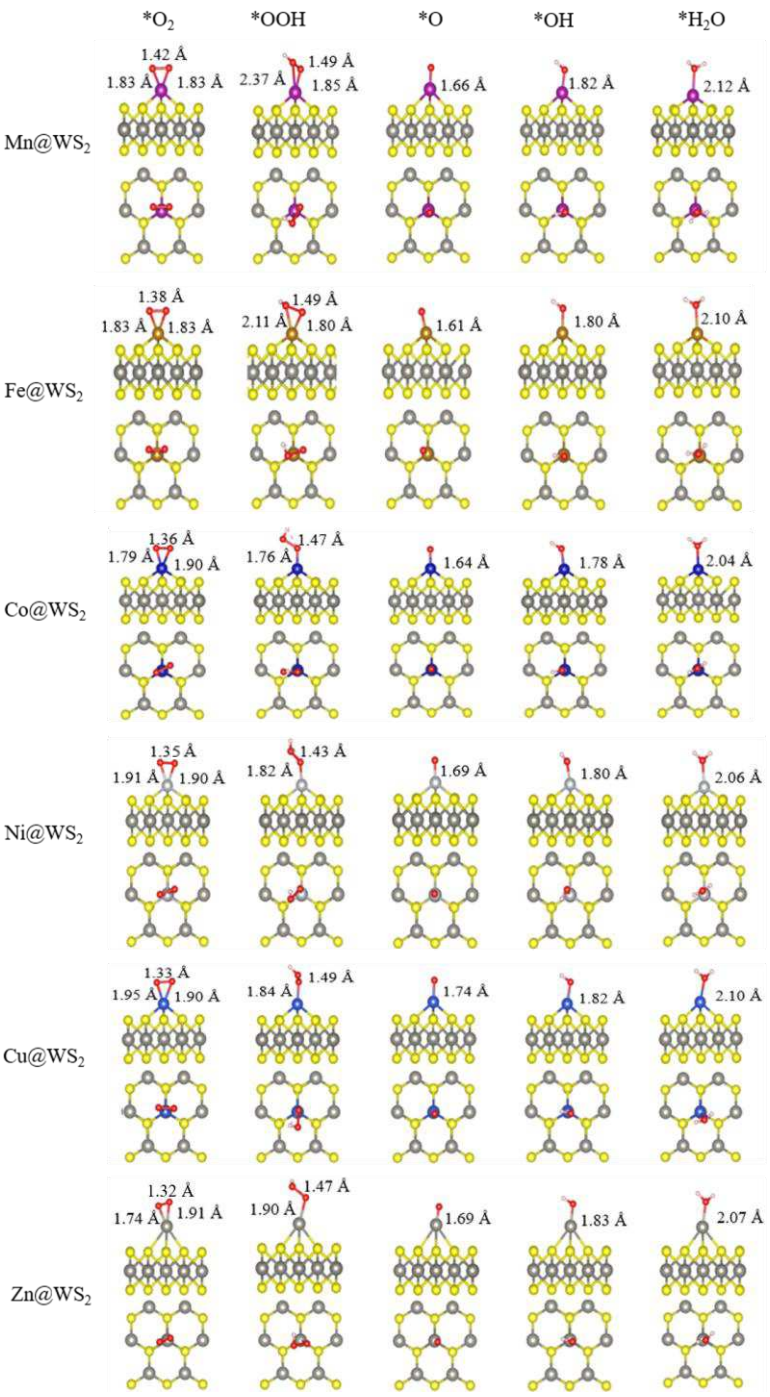

Figure. 2 The most stable structures of various intermediates adsorbed on different catalysts.

An important factor in the design of catalysts is the determination of descriptors. The Sabatier principle in heterogeneous catalysis indicates that

an ideal catalyst should bind molecules and intermediates, such as*O, *OH, and *OOH, that are neither too strong nor too weak [34]. The calculated adsorption free energies are shown in Table 2. Notably, all concerned oxygenated intermediates (*O, *OH, and *OOH) are moderately adsorbed onto the Ni@WS_2 and Zn@WS_2 catalysts. Meanwhile, the adsorption free energy is either too strong or too weak for the oxygenated species on other *M*@WS_2 (*M* = Mn, Fe, Co, and Cu) catalysts. As a result, the Ni@WS_2 and Zn@WS_2 catalysts are expected to present smaller overpotentials than others. Furthermore, one can see that the adsorption energies of intermediates in multistep reactions are nearly correlated with each other, exhibiting a linear so-called scaling relation as,

$$\Delta G_{*OOH} = (0.93 \pm 0.09)\Delta G_{*OH} + (3.33 \pm 0.13) \quad (22)$$

$$\Delta G_{*O} = (1.25 \pm 0.28)\Delta G_{*OH} + (1.49 \pm 0.20) \quad (23)$$

As displayed in Figure 3, we can see that a better linear correlation of ΔG_{*OOH} *vs*. ΔG_{*OH} than that of ΔG_{*O} *vs*. ΔG_{*OH}, indicating that ΔG_{*OH} can be regarded as a descriptor. Additionally, it is worthy of noting that the slope (0.93±0.09) of the linear scaling of ΔG_{*OOH} *v*s. ΔG_{*OH} is different from that (1.25±0.28) of ΔG_{*O} *vs*. ΔG_{*OH}, which is probably related to the difference of the local bonding states around the active metal center. For example, the slope (0.93±0.09) of is very close to 1 for the linear correlation of ΔG_{*O} *vs*. ΔG_{*OH}, indicating that both the adsorbates of *OOH and *OH mainly form an

oxygen-metal single bond while *O binds to the catalyst through a double bond.

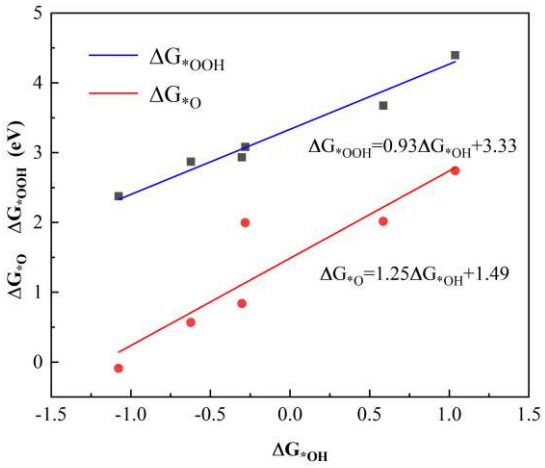

Figure. 3 Linear scaling relationships between ΔG_{*OOH} or ΔG_{*O}, and ΔG_{*OH} for the *M*@WS_2 (*M* = Mn, Fe, Co, Ni, Cu, and Zn).

3.3. OER and ORR performance

3.3.1. ORR process

Typically, the Gibbs free energy diagram can be constructed from calculated values of reaction free energy change (ΔG), and the reaction step with the highest ΔG is determined as the activity-determining step (ADS), which is used to calculate the theoretical overpotential value for a reaction [37]. Thus, the ΔG of the ORR step is calculated at U = 0 V and summarized as Gibbs free energy diagram (Figure 4). As shown in Figure 4 (b-h), 1st and 3rd steps are uphill and 2nd and 4th steps are downhill for the ORR process of 2D WS_2, and the formation of *OH from *O (3rd step) is its ORR ADS due to

the largest ΔG_3 value (0.69 eV).

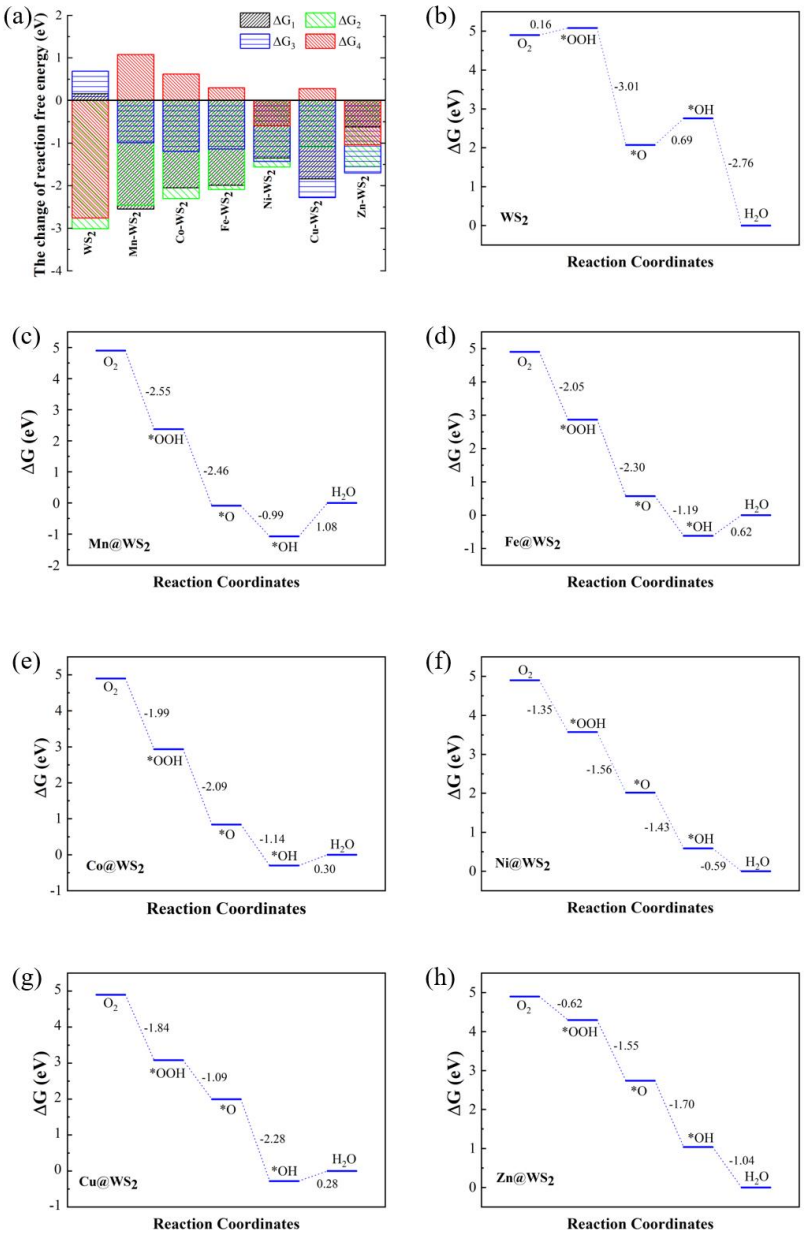

Figure. 4 (a) Changes in the reaction free energy (ΔG) and free energy diagrams calculated at U = 0 V for the ORR of *M*@WS_2 (*M* = Mn, Fe, Co, Ni, Cu, and Zn).

Furthermore, one can see that the largest ΔG_4 values of 1.08, 0.62, 0.30, 0.28, and -0.59 eV indicate that the ORR ADS is the formation of a H_2O

molecule from *OH for $Mn@WS_2$, $Fe@WS_2$, $Co@WS_2$, $Cu@WS_2$, and $Ni@WS_2$, respectively. The ORR ADS is the formation of *OOH from O_2 for $Zn@WS_2$ due to the largest ΔG_1 value of 0.62 eV. Thus, the thermodynamic overpotentials could be calculated from the obtained Gibbs free energies and they are about 1.91, 2.31, 1.85, 1.53, 1.51, 0.64, and 0.61 V for 2D WS_2, $Mn@WS_2$, $Fe@WS_2$, $Co@WS_2$, $Cu@WS_2$, $Ni@WS_2$, and $Zn@WS_2$, respectively, revealing that the ORR performance can be effectively improved by all STMA doping but Mn.

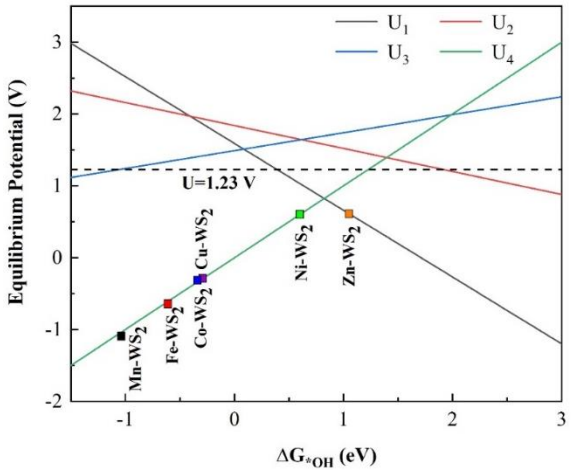

Figure. 5 The ORR thermodynamic activity volcano curve of limiting potential (U_i) *vs*. ΔG_{*OH}.

Furthermore, the thermodynamic activity volcano curves are plotted in Figure 5 to reveal the relationship between the ORR overpotential and ΔG_{*OH}. It is worthy of noticing that the standard equilibrium potentials (U_i) of steps (2)-(5) are obtained by the precondition of setting $\Delta G_i = 0$ (i = 1, 2, 3, and 4). All U_i are represented using only ΔG_{*OH} in combination with the linear

relationships with ΔG_{*OOH} and ΔG_{*O} expressed by Eqn. (22) and (23). Therefore, the specific model relations are obtained defined by Eqn. (24)-(27), which yield the correlation of the ORR overpotential with ΔG_{*OH}.

$$eU_1 = 1.59 - 0.93\Delta G_{*OH} \quad (24)$$

$$eU_2 = 1.84 - 0.32\Delta G_{*OH} \quad (25)$$

$$eU_3 = 1.49 + 0.25\Delta G_{*OH} \quad (26)$$

$$eU_4 = \Delta G_{*OH} \quad (27)$$

As shown in Figure 5, if $\Delta G_{*OH} > 0.82$ eV, U_1 presents the minimum value amongst four standard equilibrium potentials, indicating that Eqn. (2) is ADS that determines the overpotential of the overall ORR. With decreasing ΔG_{*OH} (namely, increasing the adsorption strength of *OH), the reaction overpotential decreased. Especially, the ORR overpotential reaches its minimum at the cross-point, at which the curve of U_1 *vs*. ΔG_{*OH} intersects with that of U_4 *vs*. ΔG_{*OH}. If the ΔG_{*OH} value decreases further, U_4 becomes the minimum value, indicating the ADS changes to be the formation of H_2O molecule from *OH, and the reaction overpotential increases. It means that the thermodynamic activity volcano curve (as shown in Figure 5) is defined by the U_1 *vs*. ΔG_{*OH} and U_4 *vs*. ΔG_{*OH} curves at the region with weak and strong *OH adsorption, respectively. Apparently, the relative activity can be easily determined using the abovementioned thermodynamic activity volcano curve for *M*@WS_2 ORR catalysts. As a result, Ni@WS_2 and Zn@WS_2 present

relatively small overpotentials because they are located near the top of the activity volcano curve, which results in a moderate adsorption strength of *OH. On the contrary, a rather poor ORR activity is obtained for Mn@WS_2 and Fe@WS_2 due to their excessively strong *OH adsorption.

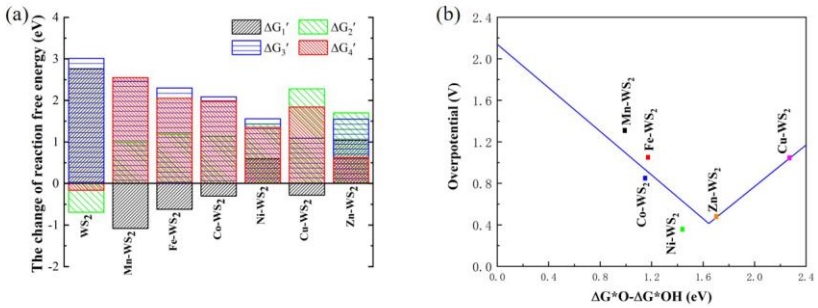

Figure. 6 (a) Changes in the reaction free energy (ΔG_i') and (b) thermodynamic activity volcano curve at U = 0 V for OER of *M*@WS_2 (*M* = Mn, Fe, Co, Ni, Cu, and Zn).

3.3.2 OER process

Similarly, the reaction free energy change at U = 0 V for OER process is depicted in Figure 6a. As depicted in the figure, the formation *OOH from *O (3rd step) is the OER ADS for the pristine 2D WS_2, Fe@WS_2, Co@WS_2, and Ni@WS_2. The 2nd step of the formation *O from *OH is the ADS for Cu@WS_2 and Zn@WS_2, while the formation of H_2O from *OOH is the ADS for Mn@WS_2. It is revealed that the OER performance is enhanced by the STMA doping in the order of 2D WS_2 < Mn@WS_2 < Fe@WS_2 < Cu@WS_2 < Co@WS_2 < Zn@WS_2 < Ni@WS_2 in terms of thermodynamics. Besides, (ΔG_{*O}-ΔG_{*OH}) has been identified as a descriptor to indicate the dependence

of the OER overpotential on (ΔG_{*O}-ΔG_{*OH}) (Figure 6b). Firstly, an inverted thermodynamic activity volcano curve can be observed, which can be applied to predict the thermodynamic activity of OER performance. One can see that Zn@WS_2 and Ni@WS_2 locate near the valley of the inverted volcano curve, indicating that they might exhibit good OER activity. In detail, the overpotentials are about 1.78, 1.32, 1.07, 1.05, 0.86, 0.47, and 0.33 V for 2D WS_2, Mn@WS_2, Fe@WS_2, Cu@WS_2, Co@WS_2, Zn@WS_2, and Ni@WS_2, respectively. In particular, a surprisingly low potential of 0.33 V is obtained for Ni@WS_2, which is better than that of the best-reported electrocatalyst IrO_2 (0.4 V) [38] and approves its superior OER electrocatalytic activity. The unusually high overpotential rules out Mn, Fe, Co, and Cu doped 2D WS_2 serving as OER catalysts, inferring that either *OH is difficult to be formed from or it cannot proceed to form *OOH easily when the adsorption of oxygen on the catalyst surface is too weak or too strong, respectively. In other words, too strong or too weak adsorption of the oxygenated adsorbates is detrimental to promote the OER activity. Hence, evaluating a thermodynamic activity volcano curve is an effective way to screen out new potential catalysts. Additionally, the Pourbaix diagram, the external potential (U_{RHE}) as a function of pH value, is theoretically calculated by using Nernst equation [39] and

depicted in Figure 7.

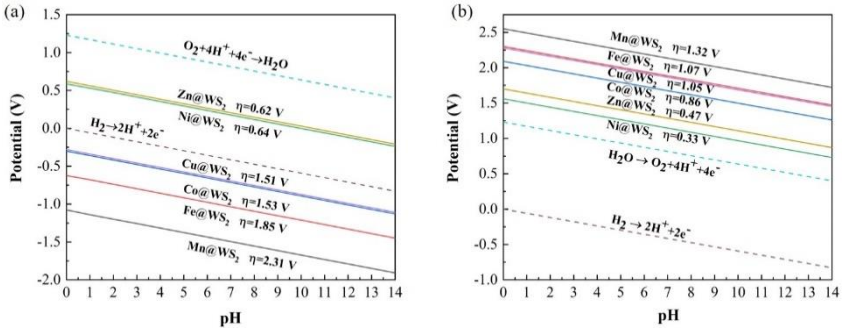

Figure. 7 The Pourbaix diagrams of the ORR (a) and OER (b) for the *M*@WS_2 (*M* = Mn, Fe, Co, Ni, Cu, and Zn). For comparison, the reversible

3.4. Electronic properties

To better understand how the impact of the STMA doping on ORR/OER activation, the electronic properties are further computationally analyzed. As an example, the density of states (DOS) of the pristine and Ni-doped 2D WS_2 are compared and shown in Figure 8. As seen, in pristine 2D WS_2 the DOSs are mainly originated from W 5*d* and S 3*p* states in either valence or conduction bands within the energy range from -7 to +3 eV, whilst a strong hybridization between W 5*d* and S 3*p* states can be observed, revealing the nature of the covalent bonding between W and S atoms. The Fermi level (E_F) is positioned within a band gap of around 1.63 eV. There is no state around E_F, indicating that the surface of pristine 2D WS_2 tends to be inert and unfavorable for the further protonation of oxygen species. In contrast, the impurity peak, mainly comprising 3*d* states of transition metal atom, usually

appears near E_F in the DOS for most doped 2D WS_2 materials. Therefore, a distinct decrease in the band gap occurs. Taking Ni@WS_2 as an example (Figure 8b), Ni doping introduces some states at the top of the valence bands, meanwhile, W 5*d* and S 3*p* states move towards lower energies a little bit, resulting in a reduced band gap compared to that of the pristine 2D WS_2. We know that a small band gap means that the electrons are easily excited from the valence to the conduction bands. Thus, decreasing band gap can effectively increase carrier concentration and the electronic conductivity, promoting the ORR/OER performances.

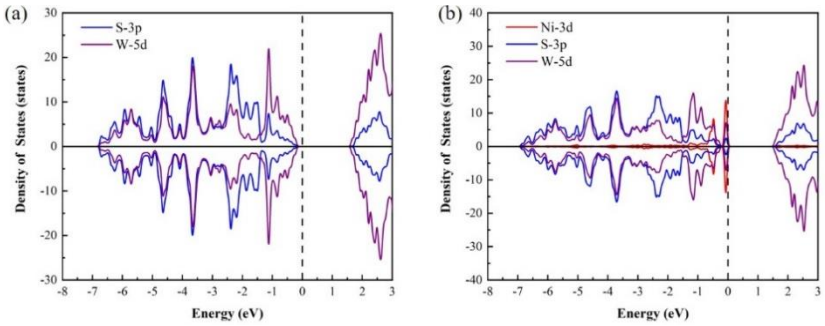

Figure. 8 The DOSs of (a) 2D WS_2 and (b) Ni@WS_2

Furthermore, we know that the electronic interaction between the oxygenated adsorbate valence states and the STMA *d* states gives rise to the bonding and antibonding states, and the electron filling of the antibonding states reflects adsorbate–metal bond strength. The well-established *d*-band center theory is an outstanding descriptor that links the electronic structure to adsorption strength, and finally to catalytic activity [40]. As depicted in

Figure 9, a roughly linear scaling correlation between the adsorption free energy ΔG_{*ads} of different oxygenated intermediates and *d*-band center (E_d) can be verified. One can see that the E_d moves gradually towards E_F from Zn to Mn, resulting in an increase of the adsorption interaction between the metal atom and the oxygenated adsorbates. In other words, with respect to E_F, the higher is the E_d, the stronger is the adsorption ability with the oxygenated adsorbates, and more difficult is the desorption of the reaction products. The specific E_d of Ni@WS_2 corresponds to the moderate adsorption for the oxygenated adsorbates (neither too strong nor too weak) compared to other catalysts, giving rise to the lowest overpotential for OER. It indicates that the ORR/OER overpotentials are correlated to the E_d and a good catalytic activity could be achieved for the catalyst with the moderate value of E_d, corresponding to the moderate adsorption for the oxygenated adsorbates.

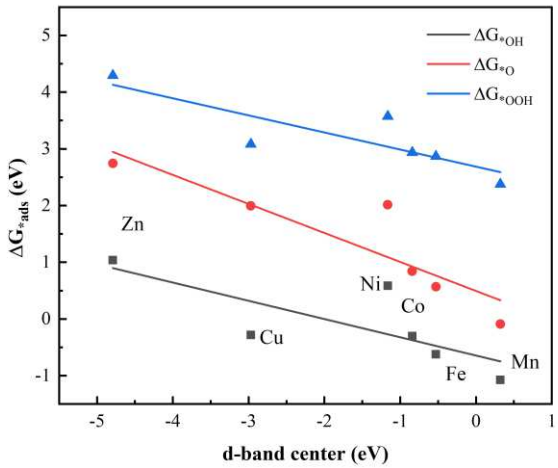

Figure. 9 The adsorption free energies of reaction intermediates as a function of the *d*-band center energy for the *M*@WS_2 (*M* = Mn, Fe, Co, Ni, Cu, and Zn).

It is known that the adsorption energy of adsorbate is dominated by the local density of states at the catalyst surface. To deeply comprehend the activation of the oxygenated adsorbates (such as $*O_2$ and *OH) by transition metal atom, the spin polarized PDOSs are computed for Ni@WS_2. As depicted in Figure 10 (a-d), the Ni dopant efficiently captures O_2 and OH through the hybridization between the oxygenated adsorbates such as $*O_2$ or *OH species and Ni 3*d* orbital. The corresponding hybridization validates possible charge transfer between the highly active partially occupied *d*-orbital of Ni atom to the half-filled O 2*p* orbital, activates the adsorption of $*O_2$ or *OH on Ni@WS_2, and benefits its catalytic activity. In addition, to clarify the charge transfer, the charge density difference, taking *OH-Ni@WS_2 as an example, is calculated from that of individual components of Ni@WS_2 and *OH. As shown in Figure 10 (e-f), the depletion of charge at Ni atom (active site) and accumulation around O atom in *OH adsorbate are observed. A quantitative result about the transfer of charge of each atom in *OH-Ni@WS_2 composite is estimated by Bader charge analysis. The O atom in *OH is prone to gain electrons while both Ni (in Ni@WS_2) and H (in *OH) prefer to lose electrons. Thus, the net charges of 0.34|e| migrate from Ni@WS_2 to the O atom of *OH-Ni@WS_2 composite, indicating that highly efficient active Ni site promotes Ni@WS_2 to become a promising OER electrocatalyst.

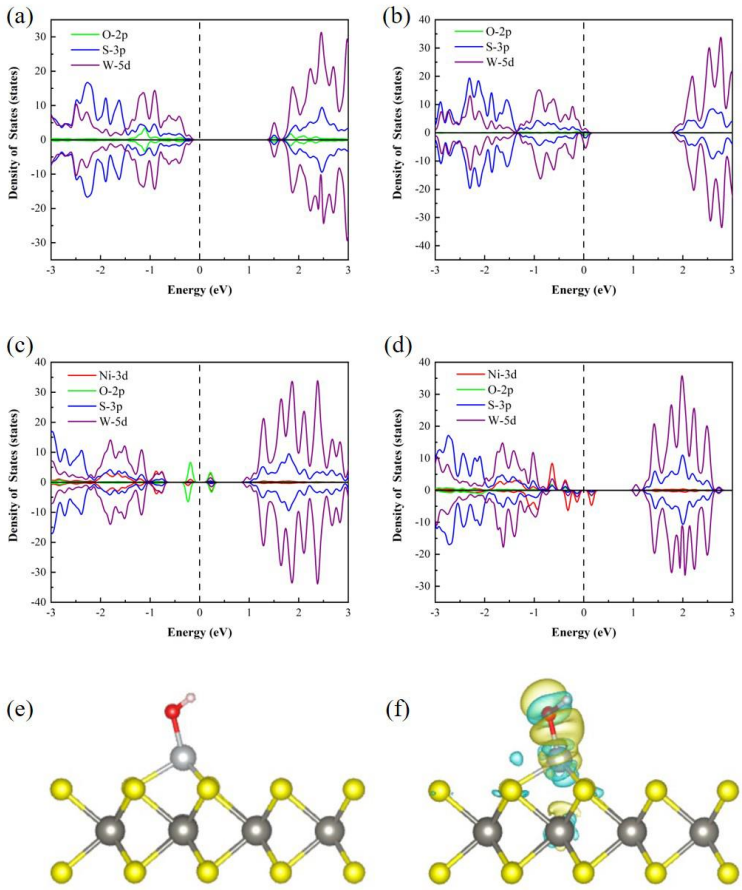

Figure. 10 DOS of the O_2 and OH (b) species absorbed on pristine 2D WS_2 (a and b) and Ni@WS_2 (c and d); (e) optimized geometry of Ni@WS_2 with *OH adsorbate, and (f) charge distributions between *OH adsorbate and Ni@WS_2. The negative (accumulation) and positive (depletion) charges are represented by cyan and yellow colors, respectively.

4. Conclusions

In summary, the catalytic activity of STMA doped *M*@WS_2 (*M* = Mn, Fe, Co, Ni, Cu and Zn) catalysts are systematically investigated using the first-principle calculations. It is revealed that the STMA doping results in a

distinct decrease in ORR and OER overpotential for almost all *M*@WS_2 catalysts compared to the pristine 2D WS_2. Especially, Ni@WS_2 and Zn@WS_2 exhibit the potential to be the good candidate of electrocatalysts toward OER processes with small overpotential compatible to the well-known precious IrO_2 catalysts. The excellent OER electrocatalytic performances for Ni@WS_2 arise due to its preferred location of the *d*-band energy center, providing the moderate adsorption of oxygenated adsorbates and giving rise to lowest overpotentials. The present work paves the way to better design new electrocatalyst for OER process, which can be potentially employed for water splitting, fuel cells, and metal-air batteries.

Declaration of Competing Interest

The authors declare that they have no known competing financial interests or personal relationships that could have appeared to influence the work reported in this paper.

Data availability

Data will be made available on request.

References

[1] Wang K, Jiang K, Chung B, Ouchi T, Burke P J, Boysen D A, Bradwell D J, Kim H, Muecke U, Sadoway D R, Lithium–antimony–lead liquid metal battery for grid-level energy storage, Nature 514(7522), 348-350 (2014).

[2] Cheng F, Liang J, Tao Z, Chen J, Functional Materials for Rechargeable Batteries, Advanced Materials 23(15), 1695-1715 (2011).

[3] Huang L-B, Zhao L, Zhang Y, Luo H, Zhang X, Zhang J, Pan H, Hu J-S, Engineering carbon-shells of M@NC bifunctional oxygen electrocatalyst towards stable aqueous rechargeable Zn-air batteries, Chemical Engineering Journal 418, 129-409 (2021).

[4] Chen Z-F, Lin X, Xia H, Hong Y, Liu X, Cai S, Duan J-N, Yang J, Zhou Z, Chang J-K, Zheng M, Dong Q, A functionalized membrane for lithium–oxygen batteries to suppress the shuttle effect of redox mediators," Journal of Materials Chemistry A 7(23), 14260-14270 (2019).

[5] Wang J, Liu W, Luo G, Li Z, Zhao C, Zhang H, Zhu M, Xu Q, Wang X, Zhao C, Qu Y, Yang Z, Yao T, Li Y, Lin Y, Wu Y, Li Y, Synergistic effect of well-defined dual sites boosting the oxygen reduction reaction, Energy & Environmental Science 11(12), 3375-3379 (2018).

[6] Huang K, Xu Y, Song Y, Wang R, Wei H, Long Y, Lei M, Tang H, Guo J, Wu H, $NiPS_3$ quantum sheets modified nitrogen-doped mesoporous carbon

with boosted bifunctional oxygen electrocatalytic performance, Journal of Materials Science & Technology 65, 1-6 (2021).

[7] Peng X, Zhang L, Chen Z, Zhong L, Zhao D, Chi X, Zhao X, Li L, Lu X, Leng K, Liu C, Liu W, Tang W, Loh K P, Hierarchically Porous Carbon Plates Derived from Wood as Bifunctional ORR/OER Electrodes, Advanced Materials, 31(16), 1900341 (2019).

[8] Zhang M, Zou L, Yang C, Chen Y, Shen Z, Bo C, An all-nanosheet OER/ORR bifunctional electrocatalyst for both aprotic and aqueous Li–O_2 batteries, Nanoscale, 11(6), 2855-2862 (2019).

[9] Ma Y, Jin F, Hu Y H, Bifunctional electrocatalysts for oxygen reduction and oxygen evolution: a theoretical study on 2D metallic WO_2-supported single atom (Fe, Co, or Ni) catalysts, Physical Chemistry Chemical Physics, 23(24), 13687-13695 (2021).

[10] Debe M K, Electrocatalyst approaches and challenges for automotive fuel cells, Nature, 486(7401), 43-51 (2012).

[11] Wang Y-J, Zhao N, Fang B, Li H, Bi X T, Wang H, Effect of different solvent ratio (ethylene glycol/water) on the preparation of Pt/C catalyst and its activity toward oxygen reduction reaction, RSC Advances, 5(70), 56570-56577 (2015).

[12] Guo S, Zhang S, Sun S, Tuning Nanoparticle Catalysis for the Oxygen Reduction Reaction, Angewandte Chemie International Edition, 52(33), 8526-8544 (2013).

[13] Cui C, Gan L, Li H-H, Yu S-H, Heggen M, Strasser P, Octahedral PtNi Nanoparticle Catalysts: Exceptional Oxygen Reduction Activity by Tuning the Alloy Particle Surface Composition, Nano Letters, 12(11), 5885-5889 (2012).

[14] Qiao B, Wang A, Yang X, Allard L F, Jiang Z, Cui Y, Liu J, Li J, Zhang T, Single-atom catalysis of CO oxidation using Pt_1/FeOx, Nature Chemistry, 3(8), 634-641 (2011).

[15] Li J, Chen M, Cullen D A, Hwang S, Wang M., Li B, Liu K, Karakalos S, Lucero M, Zhang H, Lei C, Xu H, Sterbinsky G E, Feng Z, Su D, More K L, Wang G, Wang Z, Wu G, Atomically dispersed manganese catalysts for oxygen reduction in proton-exchange membrane fuel cells, Nature Catalysis, 1(12), 935-945 (2018).

[16] Deng D, Chen X, Yu L, Wu X, Liu Q, Liu Y, Yang H, Tian H, Hu Y, Du P, Si R, Wang J, Cui X, Li H, Xiao J, Xu T, Deng J, Yang F, Duchesne P N, Zhang P, Zhou J, Sun L, Li J, Pan X, Bao X, A single iron site confined in a graphene matrix for the catalytic oxidation of benzene at room temperature, Science advances, 1(11), 1500462 (2015).

[17] Liu L, Liu S, Li L, Qi H, Yang H, Huang Y, Wei Z, Li L, Xu J, Liu B, A general method to construct single-atom catalysts supported on N-doped graphene for energy applications, Journal of Materials Chemistry A, 8(13), 6190-6195 (2020).

[18] Wang T, Yang R, Shi N, Yang J, Yan H, Wang J, Ding Z, Huang W, Luo Q, Lin Y, Gao J, Han M, Cu, N-Cooped Carbon Nanodisks with Biomimic Stomata-Like Interconnected Hierarchical Porous Topology as Efficient Electrocatalyst for Oxygen Reduction Reaction, Small, 15(43): 1902410 (2019).

[19] Li J, Chen S, Yang N, Deng M, Ibraheem S, Deng J, Li J, Li L, Wei Z, Ultrahigh-Loading Zinc Single-Atom Catalyst for Highly Efficient Oxygen Reduction in Both Acidic and Alkaline Media, Angewandte Chemie International Edition, 58(21), 7035-7039 (2019).

[20] Lin J, Wang A, Qiao B, Liu X, Yang X, Wang X, Liang J, Li J, Liu J, Zhang T, Remarkable Performance of Ir_1/FeO_x Single-Atom Catalyst in Water Gas Shift Reaction, Journal of the American Chemical Society, 135(41), 15314-15317 (2013).

[21] Yang S, Chung D Y, Tak Y-J, Kim J, Han H, Yu J-S, Soon A, Sung Y-E, Lee H, Electronic structure modification of platinum on titanium nitride resulting in enhanced catalytic activity and durability for oxygen reduction

and formic acid oxidation, Applied Catalysis B: Environmental, 174-175, 35-42 (2015).

[22] Gao C, Rao D, Yang H, Yang S, Ye J, Yang S, Zhang C, Zhou X, Jing T, Yan X, Dual transition-metal atoms doping: an effective route to promote the ORR and OER activity on MoTe2, New Journal of Chemistry, 45(12), 5589-5595 (2021).

[23] Kibsgaard J, Chen Z, Reinecke B N, Jaramillo T F, Engineering the surface structure of MoS_2 to preferentially expose active edge sites for electrocatalysis, Nature Materials, 11(11), 963-969 (2012).

[24] Lai F, Zong W, He G, Xu Y, Huang H, Weng B, Rao D, Martens J A, Hofkens J, Parkin I P, Liu T, N_2 Electroreduction to NH3 by Selenium Vacancy-Rich ReSe2 Catalysis at an Abrupt Interface, Angewandte Chemie International Edition, 59(32), 13320-13327 (2020).

[25] Xiong Y, Yang Y, Feng X, DiSalvo F J, Abruña H D, A Strategy for Increasing the Efficiency of the Oxygen Reduction Reaction in Mn-Doped Cobalt Ferrites, Journal of the American Chemical Society, 141(10), 4412-4421 (2019).

[26] Lu X F, Chen Y, Wang S, Gao S, Lou X W, Interfacing Manganese Oxide and Cobalt in Porous Graphitic Carbon Polyhedrons Boosts Oxygen Electrocatalysis for Zn–Air Batteries, Advanced Materials, 31(39), 1902339 (2019).

[27] Wang J N, Huang Y H, Zhu G Q, Zhang J M, Wei X M, Ma F, Interfacial defect engineering the electronic states and photocatalytic properties of blue phosphorus/WS_2 heterostructures, Journal of Alloys and Compounds, 859(5), 157873 (2021).

[28] Yu S, Kim J, Yoon K R, Jung J W, Oh J, Kim I D, Rational Design of Efficient Electrocatalysts for Hydrogen Evolution Reaction: Single Layers of WS_2 Nanoplates Anchored to Hollow Nitrogen-Doped Carbon Nanofibers, Acs Applied Materials & Interfaces, 7(51), 28116-28121 (2015).

[29] Kim M-J, Jeon S-J, Kang T W, Ju J-M, Yim D, Kim H-I, Park J H, Kim J-H, 2H-WS_2 Quantum Dots Produced by Modulating the Dimension and Phase of 1T-Nanosheets for Antibody-Free Optical Sensing of Neurotransmitters, ACS Applied Materials & Interfaces, 9(14), 12316-12323 (2017).

[30] Tian S, Deng C, Tang Y, Tang Q, Effect of Adatom Doping on the Electrochemical Performance of 1T'-MoS_2 for Oxygen Reduction Reactions, The Journal of Physical Chemistry C, 124(45), 24899-24907 (2020).

[31] Nørskov J K., Rossmeisl J, Logadottir A, Lindqvist L, Kitchin J R, Bligaard T, Jónsson H, Origin of the Overpotential for Oxygen Reduction at a Fuel-Cell Cathode, The Journal of Physical Chemistry B, 108(46), 17886-17892 (2004).

[32] Delley B, From Molecules to Solids with the $DMol_3$ Approach, The Journal of Chemical Physics, 113, 7756-7764 (2000).

[33] Perdew J P, Burke K, Ernzerhof M, Generalized Gradient Approximation Made Simple, Physical Review Letters, 77(18), 3865-3868 (1996).

[34] Deng C, He R, Shen W, Li M, Zhang T, A single-atom catalyst of cobalt supported on a defective two-dimensional boron nitride material as a promising electrocatalyst for the oxygen reduction reaction: a DFT study, Physical Chemistry Chemical Physics, 21(13), 6900-6907 (2019).

[35] Chan A W E, Hoffmann R, Ho W, Theoretical aspects of photoinitiated chemisorption, dissociation, and desorption of oxygen on platinum (111), Langmuir, 8(4), 1111-1119 (1992).

[36] Bockris J O M, Otagawa T, The Electrocatalysis of Oxygen Evolution on Perovskites, Journal of The Electrochemical Society, 131(2), 290 (1984).

[37] Zhao J, Chen Z, Single Mo Atom Supported on Defective Boron Nitride Monolayer as an Efficient Electrocatalyst for Nitrogen Fixation: A Computational Study, Journal of the American Chemical Society, 139(36), 12480-12487 (2017)

[38] Exner K S, Over H, Kinetics of Electrocatalytic Reactions from First-Principles: A Critical Comparison with the Ab Initio Thermodynamics Approach, Accounts of Chemical Research, 50(5), 1240-1247 (2017).

[39] Asadi M, Kim K, Liu C, Addepalli A V, Abbasi P, Yasaei P, Nanostructured transition metal dichalcogenide electrocatalysts for CO_2 reduction in ionic liquid, Science, 353(6298), 467-470 (2016).

[40] Nørskov J K, Studt F, Abild-Pedersen F, Bligaard T, Fundamental concepts in heterogeneous catalysis, (John Wiley & Sons 2014)